This is a postprint version of the following published document:

Huerta, F., Pérez, J., Cóbreces, S., Rizo, M. (2018). Frequency-Adaptive Multi-Resonant LQG State-Feedback Current Controller for LCLFiltered VSCs under Distorted Grid Voltages. *IEEE Transactions on Industrial Electronics*, pp.(99), Mar. 2018.

Frequency-Adaptive Multi-Resonant LQG State-Feedback Current Controller for LCL-Filtered VSCs under Distorted Grid Voltages

Francisco Huerta, *Member, IEEE*, Jorge Pérez, Santiago Cóbreces*, Member*, *IEEE,*
Mario Rizo

Abstract— **This paper combines the well-known linear quadratic Gaussian (LQG) control and frequency-adaptive resonators and presents a frequency-adaptive multi-resonant LQG state-feedback current controller for LCL-filtered voltage-source converters connected to a distorted grid. The paper also provides a design guideline and procedure based on robust control criteria which, in combination with the linear quadratic regulator (LQR) technique, offers flexibility in the control structure and automatizes the design of the controller. The frequency-adaptive resonators, based on second-order IIR resonators and on an on-line tuning algorithm, and the robustness criteria considered for the design process offer robustness in the face of grid voltage disturbances. The controller is evaluated and validated in a 9-kVA VSC setup configured as a rectifier.**

Index Terms— **Grid-connected converter, LCL filter, state-space current control, digital control, frequency adaptive, multi-resonant controller, harmonic mitigation.**

I. INTRODUCTION

EVOLUTION of power systems toward a model based on distributed power generation systems (DPGS) has as one of key pillars the use of power electronics interfaces, integrating renewable energy resources and electrical energy storage into the grid or feeding industrial, commercial, residential and transport applications. This changes the nature of the electrical loads from inductive and resistive to capacitive and nonlinear [1] and impacts on power quality issues, especially harmonics, which becomes a concern in low- and medium-voltage distribution networks [2].

In the scientific literature, there are three main groups of solutions for harmonic rejection: repetitive controllers, resonant controllers and grid-voltage feedforward controllers. Repetitive controllers [3] offer a low complex solution for compensating multiple harmonics. However, they may amplify high-frequency disturbances [4], do not guarantee stability by themselves being necessary to use an additional controller and the behavior of the system phase is critical [5]. Conversely, resonant controllers allow performing a selective harmonic compensation. Operating in stationary (StRF) or synchronous reference frame (SRF) (or mixed), they are mainly based on the use of continuous second-order generalized integrators (SOGI) [6], [7] or reduced-order generalized integrators (ROGI) [8]. The main drawbacks of resonant controllers is the stability issues that appears due to the phase lagging when compensating high-order harmonics what reduces the number of resonators that can be used [5]. The third group of algorithms is based on the feedforward of the grid voltage [9] and its main drawbacks are the introduction of multiple derivative terms that makes difficult its implementation and its sensitivity to weak-grid conditions [10]. To overcome those drawbacks, adaptive solutions based on impedance shaping methods have been proposed [10], [11], although they are still limited to low-order harmonics.

Grid codes require continuous operation for a frequency band around the nominal system frequency, (49-51 Hz) in 50-Hz systems, and to keep on operating during short periods of time in a wider band (47-53 Hz) [12]. In harmonic controllers, those frequency deviations affect the control performance and degrade the power quality. Frequency-adaptive solutions avoid that issue [13]. Frequency-adaptive repetitive controllers based on variable sampling frequency [14] or fractional delays [15] have been proposed. In respect to frequency-adaptive resonant controllers, in [16] a StRF ROGI-based state-feedback current control was proposed for controlling an L-filtered VSC. Other frequency-adaptive controllers proposed for L-filtered VSC considered the use of continuous-time SOGI resonators [17] or a digital implementation based on a first-order Taylor series [18]. Considering LCL-filtered VSC, [19] proposed a StRF frequency-adaptive resonant controller based on IIR Schur-lattice filter structures.

The linear quadratic regulator (LQR) or the linear quadratic Gaussian (LQG) control, when combining the former with a Kalman Filter (KF) to reduce the number of sensors, are well-

F. Huerta is with the Electronic Technology Department, Universidad Carlos III de Madrid, Leganes, 28911, Spain (e-mail: fhuerta@ing.uc3m.es).

J. Pérez and M. Rizo are with Gamesa Electric, Coslada, 28823, Spain (e-mail: jorge.perez@depeca.uah.es, mrizo@gamesacorp.com).

S. Cóbreces is with the Department of Electronics, Universidad de Alcalá, Alcalá de Henares, 28871, Spain (e-mail: cobreces@depeca.uah.es).
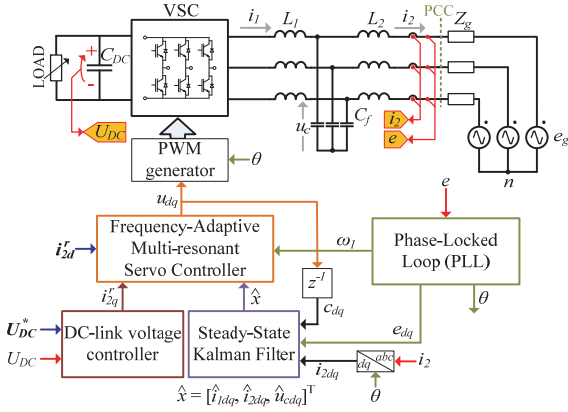
Fig. 1. General diagram of the grid-connected VSC and the proposed control scheme.
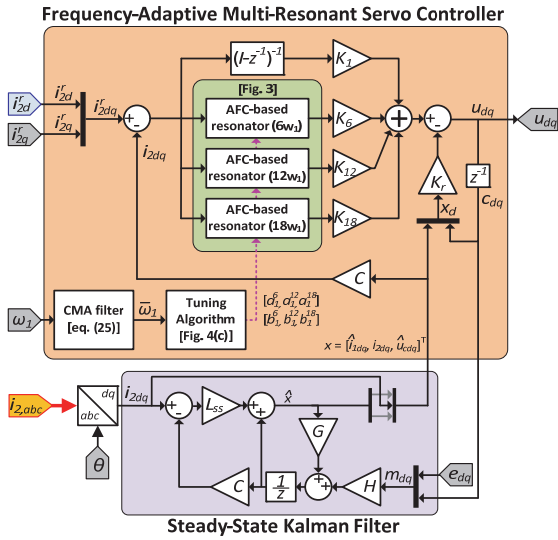

Fig. 2. Detailed diagram of the proposed control structure based on a frequency-adaptive multi-resonant LQG state-feedback controller.

known techniques in current control, being reported their use in state-feedback controllers [20]-[26] and in resonant controllers [27], [28]

In this paper, a frequency-adaptive multi-resonant LQG state-feedback current control based on second-order digital IIR resonators is proposed for the control of grid-connected LCL-filtered VSCs as depicted in Fig. 1 and detailed in Fig. 2. In addition, the paper presents design criteria that combine the LQR and the output sensitivity function in order to simplify the design of robust discrete-time multi-resonant controllers.

The two main contributions of the article are: firstly, the combinations of the well-known LQG control paradigm and the frequency-adaptive resonators in order to offer a multi-resonant controller robust to grid frequency variations. Secondly, to provide a design guideline and procedure based on robust control criteria which, in combination with the LQR technique, offers flexibility in the control structure and automatizes the design of the controller. The LQR technique provides robustness against system parameter uncertainties, while the output sensitivity function criteria provide robustness in the face of grid voltage disturbances as it will be explained in detail in section IV. Moreover, the use of frequency-adaptive resonators offers system robustness

against grid frequency variations.

Other interesting characteristics of the proposed frequency-adaptive controller are:

- The incorporation of supplementary resonator blocks in the controller will not modify significantly the control structure or the design process due to their flexibility.
- The active damping is implicit [29], because the degrees of freedom of the proposed full-state feedback controller are equal to the number of poles in the system, so the control can move any pole of the system to any position. The controller can move the LCL-filter resonance inward the unit circle damping the resonance.
- Designing directly a discrete-time resonator avoids some issues associated with the discretization of the continuous-time resonators. Not considering the computational delay may affect the system performance and stability and an inappropriate discretization process might modify pole and zero mapping, and not guaranteeing infinite gain at the desired frequency and affecting the stability [30].
- The proposed frequency-adaptive second-order IIR resonators are implemented as Transpose-Direct-Form-II (TDF-II) and were designed based on the concept of the adaptive-feedforward cancellation (AFC) resonator, in which each resonator introduces a placeable zero which might increase the robustness [4].

The DC-link voltage controller and the PLL, shown in Fig. 1, are out of the scope of this article. It is important to remark that their effect on the stability [31], [32] have been neglected considering that both algorithms have been designed considering narrow bandwidths that limit their influence on the system passivity to a small range of low frequencies where grid instability is unlikely. The PLL is configured to align the q-axis with the PCC voltage vector (i.e. $e_d = 0$), therefore, active and reactive powers are controlled by i_q and i_d, respectively, according to $P = e_q \cdot i_q$ and $Q = e_q \cdot i_d$.

Hereinafter, Section II presents the discrete-time model of the converter. Section III describes the proposed controller. Section IV addresses the adjustment of the control gain. Section V presents a wide number of experimental results. Finally, Section VI concludes.

II. STATE-SPACE LCL-FILTERED VSC MODEL

Assuming the average switch model [33], the LCL-filter grid-connected VSC shown in Fig. 1 can be state-space modeled in SRF as

$$\begin{cases} \vec{x}'(t) = A\vec{x}(t) + B_u\vec{u}(t) + B_e\vec{e}(t) \\ y(t) = C\vec{x}(t) \end{cases} \quad (1)$$

being $\vec{x} = [i_{1d} \ i_{1q} \ i_{2d} \ i_{2q} \ u_{cd} \ u_{cq}]^{\mathrm{T}}$, $\vec{y} = [i_{2d} \ i_{2q}]^{\mathrm{T}}$,

$$A = \begin{bmatrix} \frac{-R_1}{L_1} & \omega_I & 0 & 0 & \frac{-1}{L_1} & 0 \\ -\omega_I & \frac{-R_1}{L_1} & 0 & 0 & 0 & \frac{-1}{L_1} \\ 0 & 0 & \frac{-R_2}{L_2} & \omega_I & \frac{1}{L_2} & 0 \\ 0 & 0 & -\omega_I & \frac{-R_2}{L_2} & 0 & \frac{1}{L_2} \\ \frac{1}{C_f} & 0 & \frac{-1}{C_f} & 0 & 0 & \omega_I \\ 0 & \frac{1}{C_f} & 0 & \frac{-1}{C_f} & -\omega_I & 0 \end{bmatrix} \quad (2)$$

2

$$B_u = \begin{bmatrix} \frac{1}{L_l} & 0 & 0 & 0 & 0 & 0 \\ 0 & \frac{1}{L_l} & 0 & 0 & 0 & 0 \end{bmatrix}^T \quad (3)$$

$$B_e = \begin{bmatrix} 0 & 0 & \frac{-1}{L_2} & 0 & 0 & 0 \\ 0 & 0 & 0 & \frac{-1}{L_2} & 0 & 0 \end{bmatrix}^T \quad (4)$$

$$C = \begin{bmatrix} 0 & 0 & 1 & 0 & 0 & 0 \\ 0 & 0 & 0 & 1 & 0 & 0 \end{bmatrix} \quad (5)$$

$\vec{\imath}_1 = i_{1d} + j i_{1q}$ is the converter-side current, $\vec{\imath}_2 = i_{2d} + j i_{2q}$ represents the grid-side current, $\vec{u}_c = u_{cd} + j u_{cq}$ denotes the capacitor voltage, $\vec{u} = u_d + j u_q$ is the converter average output, $\vec{e} = e_d + j e_q$ represents the point of common coupling (PCC) voltage, L_1 and R_1 are the converter-side inductance and resistance, L_2 and R_2 represent the grid-side inductance and resistance, C_f is the filter capacitance, ω_1 is the fundamental grid angular frequency and superscript T denotes transpose.

The state-space model is discretized by the zero-order hold (ZOH) method [34] considering a sample time T_s. The discrete-time model of the LCL-filtered VSC is then

$$\begin{cases} \vec{x}_{k+1} = G\vec{x}_k + H_u \vec{u}_k + H_e \vec{e}_k \\ y_k = C\vec{x}_k \end{cases} \quad (6)$$

where G, H_u and H_e matrices are, respectively, the discretized A, B_u and B_e matrices.

Considering the PCC voltage as a disturbance and modeling the inherent computational delay as an additional states according to

$$\vec{c}_k = \vec{u}_{k-1} \quad (7)$$

the extended converter model is given by [20]

$$\begin{cases} \vec{x}_{d,k+1} = G_d \vec{x}_{d,k} + H_d \vec{u}_k \\ \vec{y}_k = C_d \vec{x}_{d,k} \end{cases} \quad (8)$$

with

$$\vec{x}_d = \begin{bmatrix} \vec{x} \\ \vec{c} \end{bmatrix}, G_d = \begin{bmatrix} G & H_u \\ 0 & 0 \end{bmatrix}, H_d = \begin{bmatrix} 0 \\ I \end{bmatrix}, C_d = \begin{bmatrix} C & 0 \end{bmatrix} \quad (9)$$

III. PROPOSED CURRENT CONTROLLER

A. Digital adaptive-feedforward cancellation (AFC)

Considering backward Euler's integrators, the transfer function of a digital AFC is expressed as [4]

$$R_n(z) = g_n \frac{\cos(\varphi_n) z^2 - \cos(\omega_n T_s + \varphi_n) z}{z^2 - 2\cos(\omega_n T_s) z + 1} \quad (10)$$

where ω_n is the resonant angular frequency, g_n is the gain and φ_n is the phase of the resonator. One of the two zeros introduced by the AFC depends on φ_n and has a direct influence over the robustness of the system. Considering a low g_n, phase margin is maximized if φ_n is similar to the angle of the plant at $\omega_n T_s$ [4].

The AFC can be written in state-space formulation considering the observable canonical form [35] as

$$\begin{cases} \vec{s}_{k+1} = \Phi_n^s \vec{s}_k + \Gamma_n^s \varepsilon_k \\ o_k = \begin{bmatrix} 1 & 0 \end{bmatrix} \vec{s}_k + \left(g_n \cos(\varphi_n) \right) \varepsilon_k \end{cases} \quad (11)$$

with

$$\Phi_n^s = \begin{bmatrix} 2\cos(\omega_n T_s) & 1 \\ -1 & 0 \end{bmatrix}, \Gamma_n^s = \begin{bmatrix} g_n \cos(\omega_n T_s - \varphi_n) \\ -g_n \cos(\varphi_n) \end{bmatrix} \quad (12)$$

B. Multi-resonant servo controller structure

The servo controller consists of a state-feedback regulator loop with an outer tracking loop that guarantees null tracking error to references. The proposed multi-resonant servo controller is shown in Fig. 2. The tracking loop includes a DC integrator for null tracking error at ω_1, and a bank of second-order IIR resonators based on the concept of the AFC.

Three-phase loads based on power electronics rectifiers mainly pollute grid with components of angular frequency $\pm(6h\pm1)\omega_1$ [36], which are reflected as $\pm6h\omega_1$ in SRF. The proposed controller includes three IIR resonators tuned at $6\omega_1$, $12\omega_1$ and $18\omega_1$ for compensating the harmonics -5th, 7th, -11th, 13th, -17th and 19th.

The multi-resonant state-feedback servo controller shown in Fig. 2 must be expressed in the regulator form [35] in order to apply the LQR technique and obtain the state feedback gain.

The DC integrator consists of two backward Euler integrators and can be state-space modeled as

$$\vec{x}_{1,k+1} = \Phi_1 \vec{x}_{1,k} + \Gamma_1 \vec{\varepsilon}_k \quad (13)$$

where $\vec{\varepsilon} = (\vec{y}^r - \vec{y})$ and

$$\Phi_1 = \begin{bmatrix} 1 & 0 \\ 0 & 1 \end{bmatrix}, \Gamma_1 = \begin{bmatrix} 1 & 0 \\ 0 & 1 \end{bmatrix} \quad (14)$$

The DC integrator contributes to increase the state vector of the system in two additional states, $\vec{x}_1 = [x_{1d}, x_{1q}]^T$.

The AFC-based IIR resonator for the nth harmonic is state-space modeled as

$$\vec{x}_{n,k+1} = \Phi_n \vec{x}_{n,k} + \Gamma_n \vec{\varepsilon}_k \quad (15)$$

where $\vec{x}_n = [x_{1d}^n, x_{2d}^n, x_{1q}^n, x_{2q}^n]^T$ and

$$\Phi_n = \begin{bmatrix} \Phi_n^s & 0 \\ 0 & \Phi_n^s \end{bmatrix}, \Gamma_n = \begin{bmatrix} \Gamma_n^s & 0 \\ 0 & \Gamma_n^s \end{bmatrix} \quad (16)$$

Each IIR resonator adds four additional states to the state vector of the system.

The state-space equations of the multi-resonant servo controller are rewritten as

$$\begin{cases} \vec{x}_{s,k+1} = G_s \vec{x}_{s,k} + H_s \vec{u}_k \\ \vec{y}_k = C_s \vec{x}_{s,k} \\ \vec{u}_k = -K_s \vec{x}_{s,k} \end{cases} \quad (17)$$

where $\vec{x}_s = \begin{bmatrix} \vec{x}_d^T & \vec{x}_1^T & \vec{x}_6^T & \vec{x}_{12}^T & \vec{x}_{18}^T \end{bmatrix}^T$ is of length 22 and

$$G_s = \begin{bmatrix} G_d & 0 & 0 & 0 & 0 \\ \Gamma_1 C_d & \Phi_1 & 0 & 0 & 0 \\ \Gamma_6 C_d & 0 & \Phi_6 & 0 & 0 \\ \Gamma_{12} C_d & 0 & 0 & \Phi_{12} & 0 \\ \Gamma_{18} C_d & 0 & 0 & 0 & \Phi_{18} \end{bmatrix} \quad (18)$$

$$H_s = \begin{bmatrix} H_d & 0 & 0 & 0 & 0 \end{bmatrix}^T \quad (19)$$

$$C_s = \begin{bmatrix} C_d & | & 0 & | & 0 & | & 0 & | & 0 \end{bmatrix} \quad (20)$$

$$K_s = \begin{bmatrix} K_r & | & -K_1 & | & -K_6 & | & -K_{12} & | & -K_{18} \end{bmatrix} \quad (21)$$

K_s is obtained from LQR solution for (17).

C. Frequency-adaptive implementation

Equation (10) corresponds to the transfer function of a second-order IIR filter described by

$$R_n(z) = \frac{b_0^n z^2 + b_1^n z}{z^2 + a_1^n z + a_0^n} \quad (22)$$

where

$$\begin{cases} a_1^n = -2\cos(\omega_n T_s), \, a_2^n = 1 \\ b_0^n = g_n \cos(\varphi_n), \, b_1^n = -g_n \cos(\omega_n T_s + \varphi_n) \end{cases} \quad (23)$$

The dq-axis AFC-based resonator in (15) is implemented as the dual TDF-II structure shown in Fig. 3. The only frequency-dependent coefficients are a_1^n and b_1^n, that can be rewritten as

$$\begin{aligned} a_1^n[k] &= -2\cos(\omega_n[k]T_s) \\ b_1^n[k] &= -g_n \cos(\omega_n[k]T_s + \varphi_n) \end{aligned} \quad (24)$$

where $\omega_n[k] = n\omega_1[k] = 2\pi n f_1[k]$.

The fundamental grid frequency, f_1, is extracted by a PLL algorithm and filtered by means of a Cumulative Moving Average (CMA) filter in order to eliminate oscillatory components. The equation of the implemented CMA filter is

$$\bar{f}_1[k] = \bar{f}_1[k-1] + \frac{f_1[k] - \bar{f}_1[k-1]}{N} \quad (25)$$

with $N = 1000$.

Coefficients a_1^n and b_1^n (with $n = 6, 12, 18$) in (24) must be modified according to the variations of the grid frequency in order to guarantee the harmonic rejection capabilities of the proposed current control. Both coefficients imply sinusoidal operations which might suppose excessive runtime in a direct implementation on the DSP. The optimal option in terms of processing time is to implement each coefficient as a lookup table of precalculated elements. However, that option means a trade-off between precision and memory requirement. In order to avoid those drawbacks, the proposed online tuning algorithm updates the coefficients $a_1^n[k]$ and $b_1^n[k]$ based on a piecewise first-order approximation of 7 segments.

The implemented 7-segment approximation is based on precalculating the gradients of a_1^n and b_1^n at 7 values of frequency. Defining the vector of frequencies $\vec{f} = [f_j] = [47\ 48\ 49\ 50\ 51\ 52\ 53]$ Hz where $j = 0,...,6$, the six vectors $\bar{m}_a^n$ and $\bar{m}_b^n$ are calculated, whose elements m_{aj}^n and m_{bj}^n are, respectively, the gradients of a_1^n and b_1^n at frequency f_j, according to

$$\begin{cases} m_{aj}^n = a_1^n(f_j + 0.5) - a_1^n(f_j - 0.5) \\ m_{bj}^n = b_1^n(f_j + 0.5) - b_1^n(f_j - 0.5) \end{cases} \quad (26)$$

where $a_1^n(f) = -2\cos(n\, 2\pi f\cdot T_s)$ and $b_1^n(f) = -g_n \cos(n\, 2\pi f\cdot T_s + \varphi_n)$.

The vectors $\vec{f}$, $\bar{m}_a^n$ and $\bar{m}_b^n$ are stored in the DSP memory. It is also necessary to store the vectors $\vec{a}_1^n$ and $\vec{b}_1^n$,
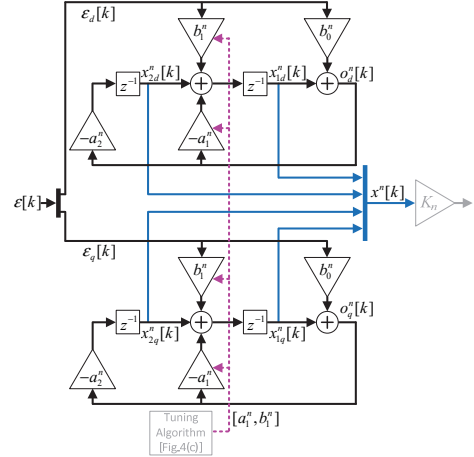

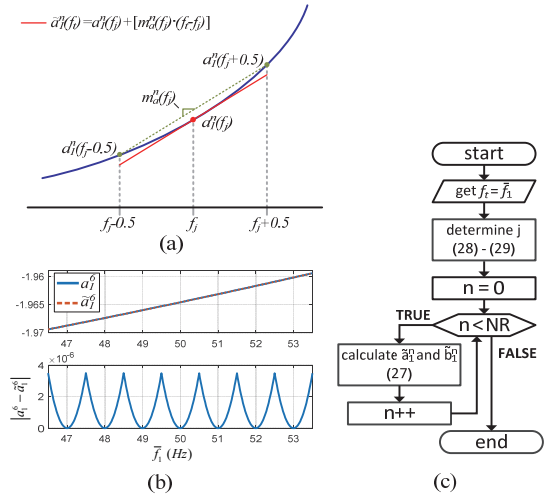Fig. 3. Dual TDF-II implementation of the AFC-based IIR resonator.

Fig. 4. (a) Implemented piecewise first-order approximation of the coefficients a_1^n and b_1^n. (b) Comparison between $\tilde{a}_1^n$ and $\tilde{b}_1^n$ and the precision error committed. (c) Flowchart of the resonator's on-line tuning algorithm.

whose elements a_{1j}^n and b_{1j}^n are equal to a_1^n and b_1^n given by (23) and evaluated with $\omega_n = 2\pi n f_j$. In total, 13 vectors of 7 elements are precalculated and stored in the DSP memory. Fig. 4(a) shows in detail the implemented approximation.

Fig. 4(c) shows the on-line tuning algorithm. The approximated coefficients are calculated according to

$$\begin{aligned} \tilde{a}_1^n[k] &= a_{1j}^n + \left(m_{aj}^n \cdot (f_t[k] - f_j)\right) \\ \tilde{b}_1^n[k] &= b_{1j}^n + \left(m_{bj}^n \cdot (f_t[k] - f_j)\right) \end{aligned} \quad (27)$$

$\tilde{a}_1^n$ and $\tilde{b}_1^n$ are periodically readjusted every T_{ta} seconds. As shown in Fig. 4(c), after getting the filtered fundamental grid frequency, $f_t = \bar{f}_1$, from the output of (25), the algorithm determines the applicable approximation segment from

$$\Delta f = f_t - 46.5 \quad (28)$$

$$j = [\Delta f] \text{ and } \begin{cases} j = 0 \text{ if } j < 0 \\ j = 6 \text{ if } j > 6 \end{cases} \quad (29)$$

where $[\cdot]$ denotes the integer part of a number. The algorithm calculates the new coefficients in a NR-iteration loop, where NR is the number of resonators.

4

Fig. 4(b) shows the precision error committed in a_1^6 when using (27) instead of (23). It can be seen as the error is lower than $4 \cdot 10^{-5}$. The precision error, $|a_1^n - \tilde{a}_1^n|$ and $|b_1^n - \tilde{b}_1^n|$, when using (27) in place of (24) is lower than $3 \cdot 10^{-5}$ in all resonators.

D. Steady-state Kalman Filter

The number of sensors required to implement a state-feedback control is reduced by means of using the so-called steady-state Kalman Filter (SSKF), which offers a performance similar to the whole KF while considerably reduces the complexity of the implementation and the computational burden [20]. The combination of LQR solution and KF is known as LQ Gaussian (LQG) control. The design of the optimal SSKF is independent of the design of the LQ servo controller according to the separation of estimation and control theorem [37].

To perform a correct estimation of the state vector, the SSKF must consider the computational delay and the PCC voltage. The model used for the design of the estimator is

$$\begin{cases} \vec{x}_{k+1} = G\vec{x}_k + H_f \vec{u}_{f,k} + \vec{w}_k \\ \vec{y}_k = C\vec{x}_k + \vec{v}_k \end{cases} \quad (30)$$

where $\vec{w}_k$ is the process noise vector with covariance matrix W, $\vec{v}_k$ is the measurement noise vector with covariance matrix V, $\vec{u}_{f,k} = [\vec{c}_k^T \mid \vec{e}_k^T]^T$ and

$$H_f = [H_u \mid H_e] \quad (31)$$

The equations of the SSKF are [20]

$$\vec{x}_{k+1}^f = G\vec{x}_k^{da} + H_f \vec{u}_{f,k} \quad (32)$$

$$\vec{x}_{k+1}^{da} = \vec{x}_{k+1}^f + L_{ss}\left(\vec{y}_{k+1} - C\vec{x}_{k+1}^f\right) \quad (33)$$

being the estimated state $\hat{x}_{k+1} \triangleq \vec{x}_{k+1}^{da}$.

The steady-state Kalman gain, L_{ss}, is calculated with

$$L_{ss} = GP_{ss}^f C^T \left(CP_{ss}^f C^T + V\right)^{-1} \quad (34)$$

after solving the algebraic Riccati equation (ARE)

$$P_{ss}^f = GP_{ss}^f G^T + W + GP_{ss}^f C^T \left(CP_{ss}^f C^T + V\right)^{-1} CP_{ss}^f G^T \quad (35)$$

Following the procedure described in [20], the matrices W and V are selected as $W = \lambda \cdot I_{6x6}$ and $V = \lambda \cdot I_{2x2}$ with $\lambda = 1$ in order to minimize the estimation bias while keeping an acceptable filtering performance.

IV. ADJUSTMENT OF THE PROPOSED CONTROLLER

The adjustment of the feedback gain might be perceived as a cumbersome task. Some authors have proposed the use of complex techniques such as genetic algorithms [38] or linear matrix inequalities (LMI) [22]. [29] proposed an interesting analytical method based on the direct pole placement to obtain the controller and observer gains in a basic servo controller structure. However, in the case of the proposed multi-resonant controller the complexity of the analytical equations dramatically increases. The attractiveness of LQR technique is that transforms the design problem into selecting intuitively the weights of two matrices, Q and R, which may facilitate designing controllers with a high number of states.

Additionally, although inferior to the well-known stability margins (infinity gain margin and 60° phase margin) in the continuous-time solution, the discrete-time LQR still provides robustness against system parameters uncertainties [39].

The LQR technique obtains K_s in (17) by solving the Ricatti's equation that minimizes a quadratic index

$$J = \frac{1}{2}\sum_{k=0}^{\infty}\left(x_k^T Q x_k + u_k^T R u_k\right) \quad (36)$$

where matrix Q weights the importance of the state variables and matrix R weights the actuation variables.

The process of choosing the weights can be automatized by using optimization techniques such as particle swarm optimization [23]. However, [24] and [20] proposed guidelines to select the Q and R weights in the multivariable current control of a LCL-filtered VSC. This paper adds some new criteria for the selection of the Q and R weights including the resonant terms and considering the maximum peak of the output sensitivity function as the figure of merit.

If considering a one degree-of-freedom (1DOF) feedback scheme [37] as the shown in Fig. 5, where G_u is the matrix of transfer functions (TFs) from u_{dq} to i_{2dq} ($G_u = C_d (zI - G_d)^{-1} H_d$), G_e is the matrix of TFs from e_{dq} to i_{2dq} ($G_e = C (zI - G)^{-1} H_e$) and K is the matrix of TFs from ε_{dq} to u_{dq}, the output sensitivity function S [37] is defined as:

$$S = \frac{i_{2dq}}{P} = (I+L)^{-1} \quad (37)$$

where P is a generalized disturbance signal ($P \equiv i_{2dq}^r \equiv -d_{dq}$), $d_{dq} = G_e \cdot e_{dq}$ and $L = G_u \cdot K$ is the loop TF. S models the effects of i_{2dq}^r and $G_e \cdot e_{dq}$ in the error ε_{dq}, which means that a low value of S implies a good tracking of the reference current and a good rejection to the grid voltage disturbances. Typically, a good robustness indicator [37] is

$$\|S(j\omega)\|_{\infty} < 6 \text{dB} \quad (38)$$

The selection guidelines in [24] and [20] suggest that the weights associated to the converter and grid currents (q_1 to q_4) should be high (beside other weights) and similar to each other. The weights of the capacitor voltage and the computational delays (q_5 to q_8) must be almost zero. The weights of the DC integrator (q_9 and q_{10}) should be fairly high, and R is associated with the limitation of the control effort.

In order to determine a criterion to select the weights associated to the resonators, a study has been carried. It is supposed that the weights associated to each resonator are similar (i.e. it is only necessary to select one weight for each resonator). Fig. 6(a) shows the output sensitivity function of the controlled system for a base set of weights where $q_1 = ... = q_4 = 1$, $q_5 = ... = q_8 = 0$, $q_9 = q_{10} = 1$, $q_{11} = ... = q_{14} = 1$, $q_{15} = ... = q_{18} = 1$, $q_{19} = ... = q_{22} = 1$ and $r_1 = r_2 = 4$. Fig. 6(b) shows the output sensitivity functions when varying q_{11} (associated to the $6\omega_1$ resonator). Fig. 6(c) presents the output
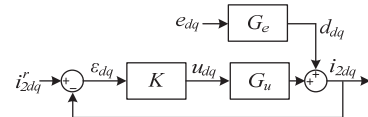

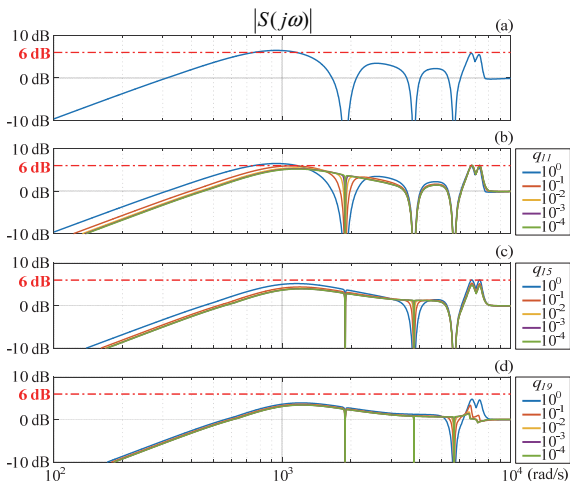Fig. 5. Block diagram of the proposed controller rearranged as a 1DOF feedback control system.

Fig. 6. Output sensitivity functions of the system: (a) with $q_1 = 1$, $q_5 = 0$, $q_9 = 1$, $q_{11} = 1$, $q_{15} = 1$, $q_{19} = 1$, $r_1 = 4$; (b) varying q_{11}; (c) varying q_{15} and $q_{11} = (0.01)^2$; (d) varying q_{19} and $q_{11} = (0.01)^2$ and $q_{15} = (0.005)^2$.

sensitivity functions when varying q_{15} and $q_{11} = (0.01)^2$. Fig. 6(d) shows the results when varying q_{19} and $q_{11} = (0.01)^2$ and $q_{15} = (0.005)^2$. It can be observed that the weight selection for the resonators is a trade-off between their bandwidth and the system robustness. Considering that grid codes do not specify harmonic limitation during transient, the recommendation is to select low weights associated to the resonators in order to guarantee robust performance. This is crucial in the $18\omega_1$ resonator as it can be seen in Fig. 6(d). The resonance angular frequency of the experimental setup is close to $18\omega_1$, so a slow resonator is chosen in order to prevent the interaction between resonator and resonance frequency, f_{res}.

Fig. 7 shows a study about the damping of the LCL-filter resonance depending on the selected r_1. It is observed that the damping increases as the chosen r_1 decreases, what means that there is a trade-off between limiting the control effort (higher r_1) and obtaining a greater resonance damping (lower r_1).

The design process consists of two LQR stages. After selecting Q and R, K_s is calculated by means of the LQR technique considering that the phases of the resonators are $\varphi_n = 0$. K_s is recalculated considering that φ_n is equal to the phase of the system formed by the extended plant (8) and the regulator loop (K_r) at $n\omega_1$.

Considering the parameters listed in Table I, the output sensitivity function obtained for the proposed multi-resonant servo controller is shown in Fig. 8. It can be seen as the output sensitivity function is less than 6 dB for the entire frequency range, which means that the designed controller is robust in the entire frequency range. The multi-loop disk gain and phase margin are GM = 8.82 dB and PM = 55.18 º at 895 Hz. Fig. 9 presents a stability analysis based on the position of the closed-loop poles of the converter and the proposed multi-resonant LQG servo controller. The poles are inside the unit circle, therefore the system is stable. The zoomed area shows that the controller moves the LCL-filter resonant poles away from the unit circle (i.e. damps the resonance).

V. EXPERIMENTAL RESULTS

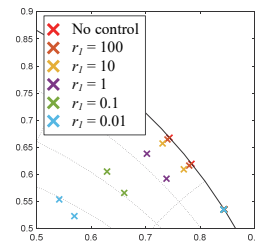The proposed current controller has been evaluated in a

Fig. 7. Effect of r_1 on the position of the LCL-filter resonant poles.
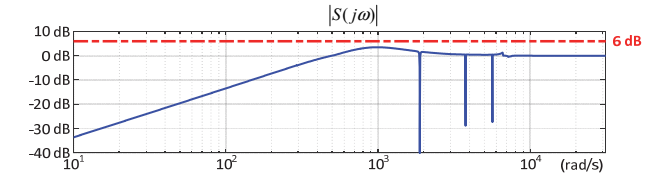

Fig. 8. Output sensitivity function of the system considering the parameters listed in Table I.
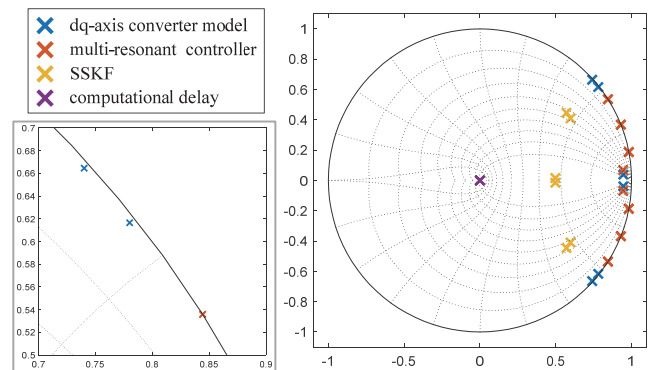

Fig. 9. Closed-loop poles of the converter controlled by the multi-resonant LQG servo controller. Zoom: resonant LCL-filter poles.
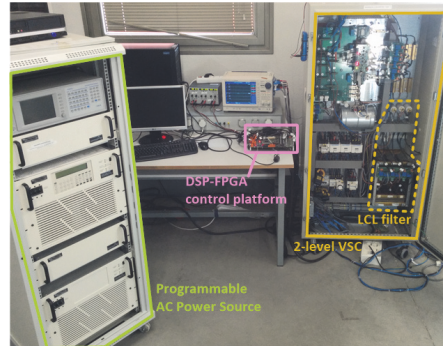

Fig. 10. Experimental setup based on a 2-level 9-kVA VSC.

VSC operating as a rectifier, although it could be also used in a VSC configured as an inverter. The experimental setup is shown in Fig. 10 and consists of a 2-level 9-kVA LCL-filter VSC interfaced with a programmable AC power source Pacific Power's 345AMX emulating the grid. The proposed current controller has been implemented on a TI DSP TMS320DSK6713. The main control and setup parameters are listed in Table. I. The sample frequency is $f_s = 10$ kHz ($T_s = 100$ μs) and the switching frequency is $f_{sw} = 5$ kHz ($T_{sw} = 200$ μs). Filter parameters and switching and sampling frequencies were chosen for complying with [36] and considering general guidelines [40] such as the level of reactive, the margin of the DC-link voltage and the location of the resonance frequency between the switching frequency and the controller bandwidth that provides certain margin against

TABLE I
EXPERIMENTAL SETUP AND CONTROL PARAMETERS

Experimental Setup					
S_n	9 kVA	L_1	3.4 mH	f_s	10 kHz
$E_{g,rms}$	110 V	R_1	28.8 mΩ	f_{sw}	5 kHz
f_1	50 Hz	L_2	1.7 mH	T_s	100 μs
U_{bc}^*	500 V	R_2	18.6 mΩ	T_{sw}	200 μs
C_{DC}	4.7 mF	C_f	18 μF	T_{ta}	2 s

AFC-based IIR resonators			
n	6	12	18
g_n	1	1	1
φ_n	-1.25 rad	-1.82 rad	-2.22 rad

Q and R weights			
$q_1, q_2, q_3, q_4, q_9, q_{10}$	10	q_5, q_6, q_7, q_8	0
$q_{11}, q_{12}, q_{13}, q_{14}$	0.01	$q_{15}, q_{16}, q_{17}, q_{18}$	0.0025
$q_{19}, q_{20}, q_{21}, q_{22}$	0.0001	r_1, r_2	100

Kalman Filter					
W	$\lambda \cdot I_{6x6}$	V	$\lambda \cdot I_{2x2}$	λ	1

TABLE II
RELATIVE VALUE OF THE CONSIDERED GRID VOLTAGE HARMONICS

-5th	7th	-11th	13th	-17th	19th
10 %	10 %	10 %	10 %	5 %	5 %

TABLE III
EXPERIMENTAL RESULTS:
RELATIVE VALUE OF THE GRID CURRENT HARMONICS

(a) Without and with resonators					
	-5th	7th	-11th	13th	-17th	19th
Resonators OFF	9.55 %	6.55 %	0.83 %	3.47 %	9.77 %	15.25 %
Resonators ON	0.21 %	0.22 %	0.44 %	0.60 %	0.75 %	1.44 %

(b) Operation with f_1 = 53 Hz (Fig. 15)					
	-5th	7th	-11th	13th	-17th	19th
Non-adaptive	9.01 %	5.69 %	0.57 %	5.02 %	14.74 %	14.27 %
Adaptive	0.21 %	0.27 %	0.51 %	0.72 %	0.98 %	1.33 %

(c) Operation with f_1 = 47 Hz (Fig. 18)					
	-5th	7th	-11th	13th	-17th	19th
Non-Adaptive	10.16 %	7.47 %	1.80 %	2.07 %	6.13 %	12.31 %
Adaptive	0.30 %	0.29 %	0.41 %	0.52 %	0.69 %	1.18 %

(d) Operation with L_g = 0.5 L_2 (Fig. 20)					
	-5th	7th	-11th	13th	-17th	19th
Resonators OFF	9.00 %	5.91 %	0.63 %	3.63 %	13.30 %	10.72 %
Resonators ON	0.28 %	0.25 %	0.44 %	0.67 %	1.14 %	1.06 %

grid impedance variations. The grid voltage has been set to 110 V_{rms} in order to avoid the connection of the output transformer in the AC power source. An additional three-phase coil of inductance value equal to the 50 % of L_2 is connected between the power source and the PCC of the converter for the experiments with grid impedance.

For the experimental tests, a distorted grid has been configured with THD_v = 21.21 % and the harmonic content listed in Table II. A high THD_v has been selected in order to test the operation of the proposed controller in an extreme distorted grid scenario. It has been considered that the converter could be also operating connected to a microgrid, where it could be possible that the 5 % THD_v limitation for network operators is not satisfied. The THD_v and THD_i are calculated up to the 50th harmonic.

Table III(a) compares the relative value of the current harmonics operating under a distorted grid without and with the resonators when i_{2d}^r = 20 A. Without harmonic compensation, the grid current is highly polluted with a

THD_i = 22.10 %. After activating the resonators, the harmonic content is significantly reduced and the converter operates with a THD_i = 2.34 % and all the considered harmonics remain within the harmonic limitations according to [36]: 5th and 7th harmonics are below 4 %, 11th and 13th harmonics are below 2 %, and 17th and 19th harmonics are below 1.5 %.

Fig. 11 and Fig. 12 evaluate the behavior of the proposed controller under steps of reactive current (i_{2d}^r = 10 A to i_{2d}^r = 20 A) and active power (P_{load} = 0.5 kW to P_{load} = 2.7 kW), respectively. The tests corroborate the correct operation and the fast dynamic of the proposed current control under active power and reactive current steps.

Fig. 13 presents the operation of a non-frequency-adaptive version of the proposed multi-resonant LQG servo controller when the fundamental frequency of the grid, f_1, changes from 50 Hz to 53 Hz. For the new frequency, the controller is unable to mitigate the current harmonics and operates with a THD_i = 24.04 %. However, the proposed frequency-adaptive multi-resonant LQG servo controller compensates the frequency variation after a transient period of time as it can be seen in Fig. 14(a) and operates with a THD_i = 2.65 %. The operation of the on-line tuning algorithm is shown in Fig. 14(b), where it can be observed as the output of the CMA filter (blue line), $\overline{f_1}$, tracks the change in the grid frequency (yellow line), f_1. The on-line tuning algorithm is executed with a period T_{ta} = 2 s, as marked by the green arrows, in which the
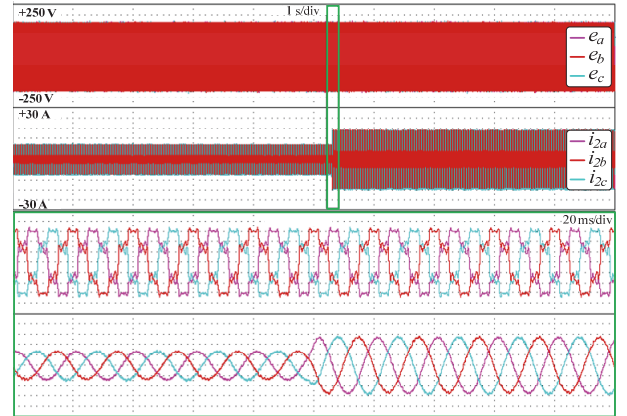

Fig. 11. Response of the frequency-adaptive multi-resonant LQG servo controller to a step of reactive current (i_{2d}^r = 10 A to i_{2d}^r = 20 A).
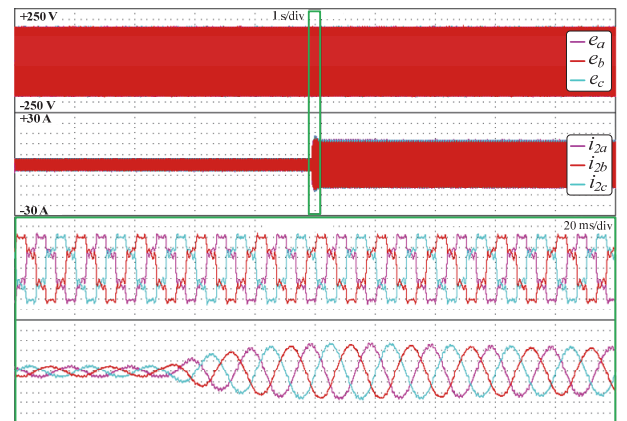

Fig. 12. Response of the frequency-adaptive multi-resonant LQG controller to a step active power (P_{load} = 0.5 kW to P_{load} = 2.7 kW).
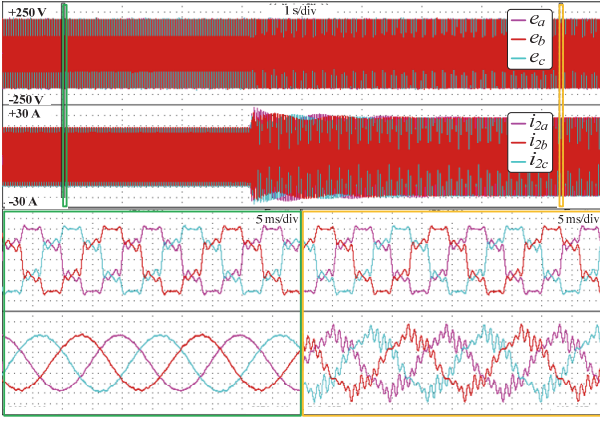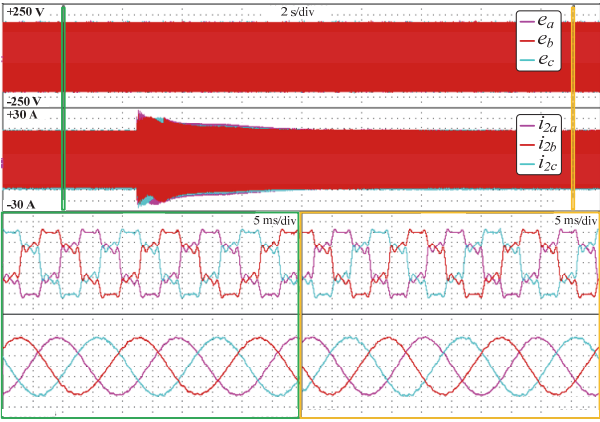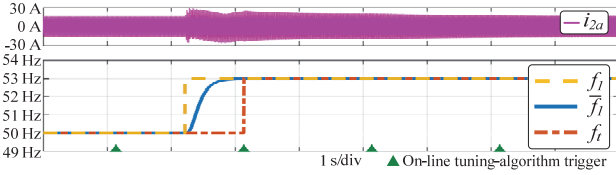
Fig. 13. Operation of a non-frequency-adaptive multi-resonant LQG servo controller under a frequency step from $f_1 = 50$ Hz to $f_1 = 53$ Hz.

(a)

(b)

Fig. 14. (a) Response of the proposed frequency-adaptive multi-resonant LQG servo controller under a grid frequency variation from $f_1 = 50$ Hz to $f_1 = 53$ Hz. (b) Operation of the on-line tuning algorithm.
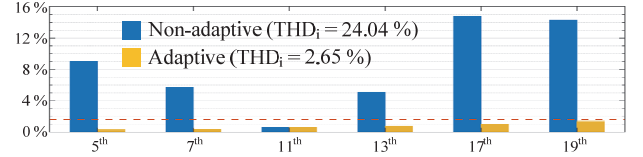

Fig. 15. Harmonic current spectrums for the non- and frequency-adaptive and the non-frequency-adaptive controllers when $f_1 = 53$ Hz.
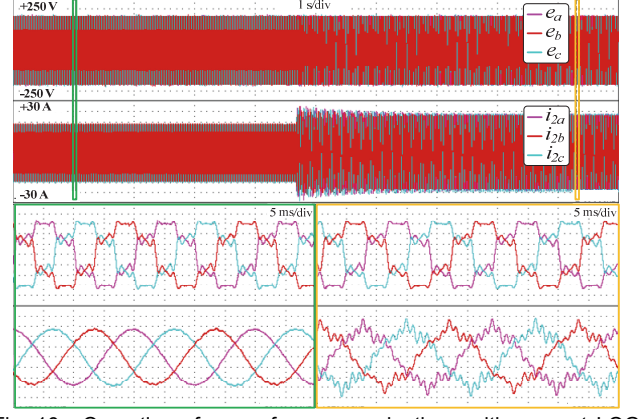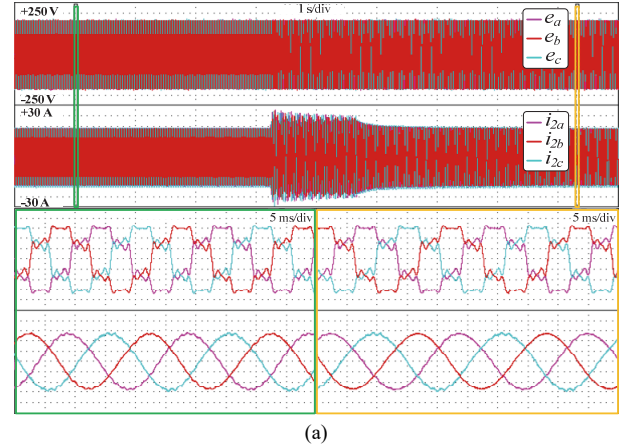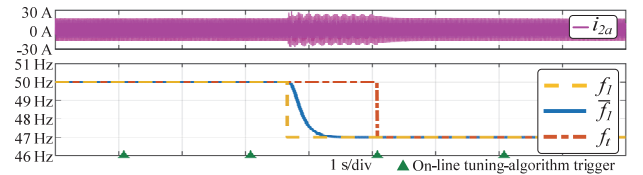

Fig. 16. Operation of a non-frequency-adaptive multi-resonant LQG servo controller under a frequency step from $f_1 = 50$ Hz to $f_1 = 47$ Hz.

(a)

(b)

Fig. 17. (a) Response of the proposed frequency-adaptive multi-resonant LQG servo controller under a grid frequency variation from $f_1 = 50$ Hz to $f_1 = 47$ Hz. (b) Operation of the on-line tuning algorithm.
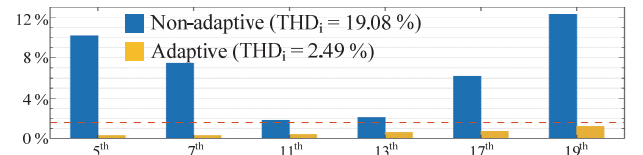

Fig. 18. Comparison of the harmonic current spectrums for the non- and frequency-adaptive controllers when $f_1 = 47$ Hz.

value of the frequency of the tuning algorithm (red line), f_t, is updated according to $f_t = \overline{f}_1$, and therefore the coefficients defined by (27) are recalculated. The current harmonic spectrums of both controllers are compared in Fig. 15 and Table III(b), where it can be observed that the frequency-adaptive controller mitigates all the considered harmonics below limitations in [36] and operates with a THD_i below the 5 %, while the non-frequency-adaptive controller does not, thus infringing the grid code requirements.

Similar results are obtained for a frequency variation from 50 Hz to 47 Hz. Fig. 16 shows as the non-frequency-adaptive controller operates with a $THD_i = 19.08$ %. In contrast, in Fig. 17 can be observed as the on-line tuning algorithm compensates the frequency variation and the converter operates with a $THD_i = 2.49$ %. Fig. 18 and Table III(c) compares the harmonic spectrum of both controllers.

Experimental results with a grid impedance equivalent to the 50 % of L_2, which implies a short-circuit ratio (SCR) equal

to 15, are presented in Fig. 19, Fig. 20 and Table III(d). It can be observed as the proposed controller mitigates the grid current harmonic content after connecting the resonators and obtains a $THD_i = 2.54$ %, substantially lower than $THD_i = 20.91$ % obtained when operating without resonators.
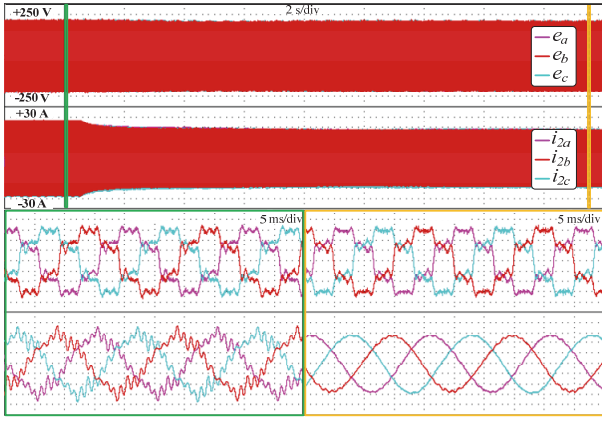
Fig. 19. Operation of the proposed frequency-adaptive multi-resonant LQG servo controller when L_g equivalent to the 50 % of L_2 before and after connecting the resonators.
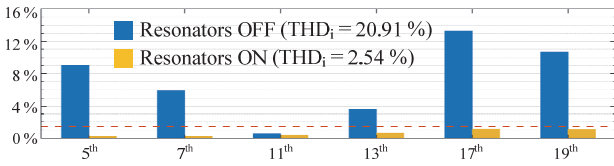

Fig. 20. Comparison of the harmonic current spectrums for the proposed frequency-adaptive multi-resonant LQG servo controller when L_g equivalent to the 50 % of L_2.

Fig. 21 shows a simulation with SCR = 10, where the controller correctly tracks a step of reactive current ($i^r_{2d} = 10$ A to $i^r_{2d} = 20$ A). An analysis of (37) as a function of SCR reveals that as SCR approaches 10, which entails f_{res} closer to 900 Hz, S becomes riskily high at 900 Hz ($18\omega_1$). Fig. 22(a) shows that the infinity norm of S, $\|S\|_\infty$, presents a maximum (i.e. a point of critical stability) at SCR = 9.72 (f_{res} = 938 Hz). Simulation results have demonstrated that the system becomes unstable when SCR < 9.72. Fig. 22(b) shows as the closed-loop pole of the $18\omega_1$ resonator goes out the unit circle when SCR < 9.72. Two options can be considered to improve the robustness. If the $18\omega_1$ resonator is turn off under low SCR, the converter is able to operate with SCR = 5 at the cost of deteriorating the power quality. The other option is to modify the values of the LCL filter in order to move f_{res} away from $18\omega_1$. Reducing L_1 by 20 % moves nominal f_{res} to 1161 Hz and the maximum of $\|S\|_\infty$ to SCR = 5.12 as Fig. 22(c) shows. In this way, robustness increases and the controller is able to overcome lower SCR as simulation tests have verified.

The robustness study has been completed with an analysis based on the location of the closed-loop poles of the controlled converter considering $L_g = 0$ and L_1 and L_2 lower than their nominal values, $L_{1,n}$ = 3.4 mH and $L_{2,n}$ = 1.7 mH. Fig. 23(a) maps the stable region of the controller (blue area) in function of L_1 and L_2. The controller is stable while $L_1 > 0.3 \cdot L_{1,n}$ for any L_2. Although the SSKF reduces the stable region as shown in Fig. 23(b), the system is still stable considering simultaneous 10 % deviations for both inductances and maximum individual variations of $L_1 > 0.75 \cdot L_{1,n}$ and $L_2 > 0.85 \cdot L_{2,n}$. Fig. 24 present the simulation results considering $L_1 = 0.9 \cdot L_{1,n}$ and $L_2 = 0.9 \cdot L_{2,n}$, where it can be observed that the system is stable and operates correctly.
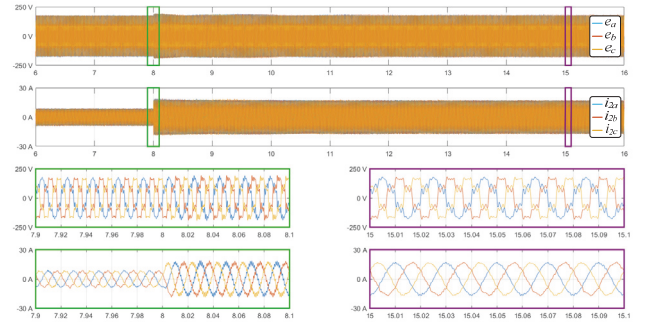

Fig. 21. Simulation results considering SCR = 10. Response to a step of reactive current (i^r_{2d} = 10 A to i^r_{2d} = 20 A).
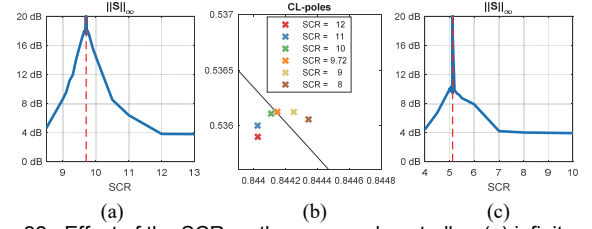

Fig. 22. Effect of the SCR on the proposed controller: (a) infinity norm of S and (b) position of the closed-loop pole of the $18\omega_1$ resonator. (c) Effect on the infinity norm of S considering $0.8 \cdot L_1$.
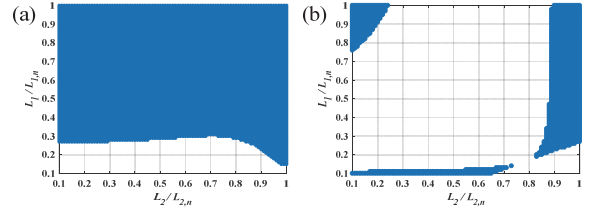

Fig. 23. Map of the stable region (blue areas) in function of L_1 and L_2 when $L_g = 0$. (a) Controller and (b) the effect of the SSKF.
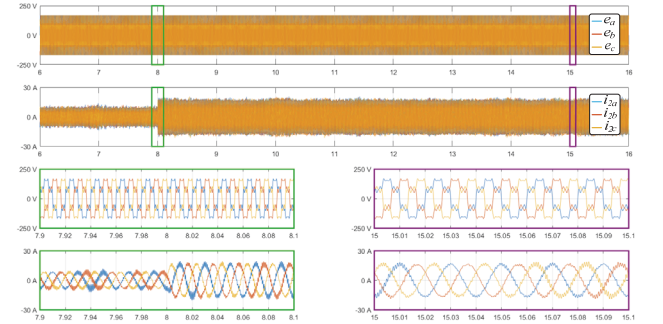
Fig. 24. Simulation results considering $L_1 = 0.9\,L_{1,n}$ and $L_2 = 0.9\,L_{2,n}$. Response to a step of reactive current (i^r_{2d} = 10 A to i^r_{2d} = 20 A).

TABLE IV
EXECUTION TIME

Full algorithm	38 µs
PLL + communications + acquisition + etc.	24 µs
Servo controller + DC control	8 µs
SSKF	4 µs
Frequency-adaptive resonators	2 µs

Table IV presents the execution time of the different routines implemented on the DSP to operate the converter. It can be observed that the computational burden of the proposed frequency-adaptive multi-resonant LQG controller supposes only the 14 % of T_s, being affordable for any present-day digital control platform commonly used in converter's control.

VI. CONCLUSIONS

This paper proposes a frequency-adaptive multi-resonant current controller for LCL-filtered VSCs. The proposed controller is based on a LQG state-feedback controller, which integrates frequency-adaptive AFC-based IIR resonators in a servo-controller structure and uses a KF to not increase the number of sensors required to perform the control. The proposed frequency-adaptive AFC-based resonators are based on an IIR-filter implementation and an on-line tuning algorithm. The two main contributions of the article are the combinations of the well-known LQG control paradigm and the frequency-adaptive resonators in order to offer a multi-resonant controller robust to grid frequency variations, and to provide a design guideline and procedure based on robust control criteria which, in combination with the LQR technique, offers flexibility in the control structure and automatizes the design of the controller. The experimental results corroborate the performance and robustness of the proposed controller under distorted grid voltages, grid-frequency variations and grid impedances. Although the implemented controller has not been designed to operate under unbalanced grids, following the proposed LQG control design process and extrapolating the control structure in order to consider the negative sequence, there would be no difficulty in designing a frequency-adaptive multi-resonant controller able to compensate unbalanced grid voltages.

REFERENCES

[1] D. Boroyevich, I. Cvetkovic, R. Burgos, and D. Dong, "Intergrid: A Future Electronic Energy Network?," *IEEE J. Emerg. Sel. Topics Power Electron.*, vol. 1, no. 3, pp. 127–138, Sep. 2013.

[2] Y. W. Li and J. He, "Distribution System Harmonic Compensation Methods: An Overview of DG-Interfacing Inverters," *IEEE Ind. Electron. Mag.*, vol. 8, no. 4, pp. 18–31, Dec. 2014.

[3] Q. C. Zhong and T. Hornik, "Cascaded Current–Voltage Control to Improve the Power Quality for a Grid-Connected Inverter With a Local Load," *IEEE Trans. Ind. Electron.*, vol. 60, no. 4, pp. 1344–1355, Apr. 2013.

[4] M. Orellana and R. Griñó, "Some considerations about discrete-time AFC controllers," in *Proc. 52nd IEEE Conf. Decision Control*, 2013, pp. 6904–6909.

[5] A. Lidozzi, C. Ji, L. Solero, P. Zanchetta and F. Crescimbini, "Resonant–Repetitive Combined Control for Stand-Alone Power Supply Units," *IEEE Trans. Ind. Appl.*, vol. 51, no. 6, pp. 4653–4663, Nov.-Dec. 2015.

[6] C. Citro, P. Siano and C. Cecati, "Designing Inverters' Current Controllers With Resonance Frequencies Cancellation," *IEEE Trans. Ind. Electron.*, vol. 63, no. 5, pp. 3072-3080, May 2016.

[7] L. F. A. Pereira, J. V. Flores, G. Bonan, D. F. Coutinho, and J. M. G. da Silva, "Multiple Resonant Controllers for Uninterruptible Power Supplies—A Systematic Robust Control Design Approach," *IEEE Trans. Ind. Electron.*, vol. 61, no. 3, pp. 1528–1538, Mar. 2014.

[8] C. A. Busada, S. Gomez Jorge, A. E. Leon, and J. A. Solsona, "Current Controller Based on Reduced Order Generalized Integrators for Distributed Generation Systems," *IEEE Trans. Ind. Electron.*, vol. 59, no. 7, pp. 2898–2909, Jul. 2012.

[9] W. Li, X. Ruan, D. Pan, and X. Wang, "Full-feedforward schemes of grid voltages for a three-phase LCL-type grid-connected inverter," *IEEE Trans. Ind. Electron.*, vol. 60, no. 6, pp. 2237–2250, Jun. 2013.

[10] J. Xu, S. Xie, Q. Qian, and B. Zhang, "Adaptive Feedforward Algorithm Without Grid Impedance Estimation for Inverters to Suppress Grid Current Instabilities and Harmonics Due to Grid Impedance and Grid Voltage Distortion," *IEEE Trans. Ind. Electron.*, vol. 64, no. 9, pp. 7574-7586, Sept. 2017.

[11] X. Li, J. Fang, Y. Tang, X. Wu, and Y. Geng, "Capacitor-Voltage Feedforward With Full Delay Compensation to Improve Weak Grids Adaptability of LCL-Filtered Grid-Connected Converters for Distributed Generation Systems," *IEEE Trans. Power Electron.*, vol. 33, no. 1, pp. 749-764, Jan. 2018.

[12] A. Etxegarai, P. Eguia, E. Torres, A. Iturregi, and V. Valverde, "Review of grid connection requirements for generation assets in weak power grids," *Renew. Sustain. Energy Rev.*, vol. 41, pp. 1501–1514, Jan. 2015.

[13] A. R. Monter, E. J. Bueno, A. García-Cerrada, F. J. Rodríguez, and F. M. Sánchez, "Detailed analysis of the implementation of frequency adaptive resonant and repetitive current controllers for grid-connected converters," *Electr. Power Syst. Res.*, vol. 116, pp. 231–242, Nov. 2014.

[14] M. A. Herran, J. R. Fischer, S. A. Gonzalez, M. G. Judewicz, I. Carugati, and D. O. Carrica, "Repetitive control with adaptive sampling frequency for wind power generation systems," *IEEE J. Emerg. Sel. Top. Power Electron.*, vol. 2, no. 1, pp. 58–69, Mar. 2014.

[15] G. Escobar, M. Hernandez-Gomez, A. A. Valdez-Fernandez, M. J. Lopez-Sanchez, and G. A. Catzin-Contreras, "Implementation of a $6n \pm 1$ repetitive controller subject to fractional delays," *IEEE Trans. Ind. Electron.*, vol. 62, no. 1, pp. 444–452, Jan. 2015.

[16] S. Gómez Jorge, C. A. Busada, and J. A. Solsona, "Frequency-Adaptive Current Controller for Three-Phase Grid-Connected Converters," *IEEE Trans. Ind. Electron.*, vol. 60, no. 10, pp. 4169–4177, Oct. 2013.

[17] L. S. Xavier, A. F. Cupertino, J. T. de Resende, V. F. Mendes, and H. A. Pereira, "Adaptive current control strategy for harmonic compensation in single-phase solar inverters," *Elect. Power Syst. Res.*, vol. 142, pp. 84–95, Jan. 2017.

[18] F. Freijedo, A. Yepes, J. Malvar, O. López, P. Fernandez-Comesana, A. Vidal, and J. Doval-Gandoy, "Frequency tracking of digital resonant filters for control of power converters connected to public distribution systems," *IET Power Electron.*, vol. 4, no. 4, pp. 454–462, Apr. 2011.

[19] F. Gonzalez-Espin, I. Patrao, E. Figueres, and G. Garcera, "An Adaptive Digital Control Technique for Improved Performance of Grid Connected Inverters," *IEEE Trans. Ind. Informat.*, vol. 9, no. 2, pp. 708–718, May 2013.

[20] F. Huerta, D. Pizarro, S. Cobreces, F. J. Rodriguez, C. Giron, and A. Rodriguez, "LQG Servo Controller for the Current Control of LCL Grid-Connected Voltage-Source Converters," *IEEE Trans. Ind. Electron.*, vol. 59, no. 11, pp. 4272–4284, Nov. 2012.

[21] R. Panigrahi, B. Subudhi, and P. C. Panda, "A Robust LQG Servo Control Strategy of Shunt-Active Power Filter for Power Quality Enhancement," *IEEE Trans. Power Electron.*, vol. 31, no. 4, pp. 2860–2869, Apr. 2016.

[22] L. A. Maccari, C. L. d. Amaral Santini, H. Pinheiro, R. C. L. F. de Oliveira, and V. F. Montagner, "Robust optimal current control for grid-connected three-phase pulse-width modulated converters," *IET Power Electron.*, vol. 8, no. 8, pp. 1490–1499, Jul. 2015.

[23] B. Ufnalski, A. Kaszewski, and L. M. Grzesiak, "Particle Swarm Optimization of the Multioscillatory LQR for a Three-Phase Four-Wire Voltage-Source Inverter With an LC Output Filter," *IEEE Trans. Ind. Electron.*, vol. 62, no. 1, pp. 484–493, Jan. 2015.

[24] E. Wu and P. W. Lehn, "Digital Current Control of a Voltage Source Converter With Active Damping of LCL Resonance," *IEEE Trans. Power Electron.*, vol. 21, no. 5, pp. 1364–1373, Sep. 2006.

[25] S. Alepuz, S. Busquets-Monge, J. Bordonau, J. Martinez-Velasco, C. Silva, J. Pont, and J. Rodriguez, "Control strategies based on symmetrical components for grid-connected converters under voltage dips," *IEEE Trans. Ind. Electron.*, vol. 56, no. 6, pp. 2162–2173, Jun. 2009

[26] C. Olalla, R. Leyva, A. E. Aroudi, and I. Queinnec, "Robust LQR control for PWM converters: An LMI approach," *IEEE Trans. Ind. Electron.*, vol. 56, no. 7, pp. 2548–2558, Jul. 2009.

[27] S. A. Khajehoddin, M. Karimi-Ghartemani and M. Ebrahimi, "Optimal and Systematic Design of Current Controller for Grid-Connected Inverters," *IEEE J Emerg Sel Top Power Electron,* to be published, doi: 10.1109/JESTPE.2017.2737987.

[28] J. Perez, S. Cobreces, F. J. Rodriguez, E. J. Bueno, I. Sanz, F. Huerta, and R. Grino "Static reference frame LQR optimal state-feedback control for static-series compensators," in *Proc. of IEEE IECON 2013*, Vienna, Nov. 2013, pp. 3776-3781.

[29] J. Kukkola, M. Hinkkanen, and K. Zenger, "Observer-Based State-Space Current Controller for a Grid Converter Equipped With an LCL Filter: Analytical Method for Direct Discrete-Time Design," *IEEE Trans. Ind. Appl.*, vol. 51, no. 5, pp. 4079-4090, Sep.-Oct. 2015.

[30] A. G. Yepes, F. D. Freijedo, J. Doval-Gandoy, Ó López, J. Malvar and P. Fernandez-Comesaña, "Effects of Discretization Methods on the Performance of Resonant Controllers," *IEEE Trans. Power Electron.*, vol. 25, no. 7, pp. 1692–1712, Jul. 2010.

[31] L. Harnefors, M. Bongiorno, and S. Lundberg, "Input-Admittance Calculation and Shaping for Controlled Voltage-Source Converters," *IEEE Trans. Ind. Electron.*, vol. 54, no. 6, pp. 3323-3334, Dec. 2007.

[32] B. Wen, D. Boroyevich, R. Burgos, P. Mattavelli, and Z. Shen, "Analysis of D-Q Small-Signal Impedance of Grid-Tied Inverters," *IEEE Trans. Power Electron.*, vol. 31, no. 1, pp. 675-687, Jan. 2016.

[33] M. Lindgren, "Modeling and Control of Voltage Source Converters Connected to the Grid," Ph.D. dissertation, Chalmers Univ. Technol., Göteborg, Sweden, 1998.

[34] W. S. Levine, *The control handbook*. Boca Raton, FL: CRC Press, 1996.

[35] K. Ogata, *Discrete-Time Control Systems*, 2nd ed. Englewood Cliffs, NJ: Prentice-Hall, 1994.

[36] *IEEE Recommended Practices and Requirements for Harmonic Control in Electrical Power Systems*, IEEE Standard 519-1992, 1993.

[37] S. Skogestad and I. Postlethwaite, *Multivariable Feedback Control*. Hoboken, NJ: Wiley, 1996.

[38] W. Lenwari, M. Sumner, and P. Zanchetta, "The Use of Genetic Algorithms for the Design of Resonant Compensators for Active Filters," *IEEE Trans. Ind. Electron.*, vol. 56, no. 8, pp. 2852–2861, Aug. 2009.

[39] U. Shaked, "Guaranteed stability margins for the discrete-time linear quadratic optimal regulator," *IEEE Trans. Autom. Control*, vol. 31, no. 2, pp. 162–165, Feb. 1986.

[40] M. Liserre, F. Blaabjerg, and S. Hansen, "Design and control of an LCL-filter-based three-phase active rectifier," *IEEE Trans. Ind. Appl.*, vol. 41, no. 5, pp. 1281-1291, Sept.-Oct. 2005.

Santiago Cóbreces (S'03–M'09) was born in Alcala de Henares, Spain, in 1980. He received the B.Sc. and the M.Sc. degree in telecom engineering and the Ph.D. degree in electronics engineering from the University of Alcalá, Alcalá de Henares, Spain, in 2003 and 2009, respectively.

Since 2012, he is an Associate Professor with the Department of Electronics, University of Alcalá, where he is a member of the Research Group "Electronics Engineering Applied to the Renewable Energies." His current research interests include automatic control and system identification applied to power electronic systems power quality, and distributed power generation systems.

Mario Rizo was born in 1986 in Madrid, Spain. He received the M.Sc. degree in telecommunication engineering and the Ph.D. degree from the University of Alcala, Alcala de Henares, Spain, in 2009 and 2013, respectively.

From 2007 to 2013, he was a member of the Electronic Engineering Applied to Renewable Energies Research Group, University of Alcala. He is currently with Gamesa Electric, Madrid, Spain. His research interests include multi-sequence control of voltage-source converters applied to renewable energy systems, energy storage systems, microgrids, and medium-voltage multilevel converters.

Francisco Huerta (S'08-M'11) received the M.Sc. degree and the Ph.D. degree in electronics engineering from the University of Alcalá, Alcalá de Henares, Spain, in 2006 and 2011, respectively.

He worked as a Research Assistant from 2007 and 2012 with the University of Alcalá. From 2013 until 2016, he was a Postdoctoral Researcher with Institute IMDEA Energy. From 2016 to 2017, he worked as a Researcher with the University of Alcalá. He is currently an Assistant Professor with the Carlos III University of Madrid. His research interests include control of power electronics converters, power quality and distributed power generation systems.

Jorge Pérez was born in Madrid, Spain, in 1988. He received both B.Sc, M.Sc and PhD degree in industrial electronics from University of Alcala (UAH), Madrid, Spain, in 2011, 2013 and 2017 respectively.

Until 2017, he was a researcher for GEISER Group of the UAH. He is currently with Gamesa Electric, Madrid, Spain. His research interests include automatic control applied to power electronic systems, power quality, and distributed power generation systems.